J Mater Sci: Mater Electron

Hydrothermal synthesis of Ce/Zr co-substituted $BiFeO_3$: *R3c*-to-*P4mm* phase transition and enhanced room temperature ferromagnetism

Zahra Adineh[1] and Ahmad Gholizadeh[1,*]

[1] School of Physics, Damghan University, Damghan, Iran

Received: 6 March 2021
Accepted: 17 September 2021

ABSTRACT

A facile hydrothermal method was used for fabricating phase-pure $Bi_{1-x}Ce_xFe_{1-x}Zr_xO_3$ (x = 0.00, 0.03, 0.06) multiferroic ferrites, and the dependence of structural, optical, and magnetic properties on the composition have been investigated. The samples were investigated by X-ray diffraction, Raman and Fourier transform infrared spectroscopies, scanning electron microscopy, UV–Vis spectroscopy, and vibrating sample magnetometer at room temperature. Structural results show that the structure of $Bi_{1-x}Ce_xFe_{1-x}Zr_xO_3$ ferrites is indexed to a rhombohedral structure with the *R3c* space group. However, the weakening in the intensity, the expansion of the line-width of all bands, and some band shifts observed in Raman spectra indicate a structural transition from rhombohedral (*R3c*) to pseudo-tetragonal (*P4mm*) phase as the content of Ce/Zr increases. Also, a significantly enhanced intensity of the A1–2 mode in Raman spectra means that there is a novel behavior of magnetic anisotropy in the Ce/Zr co-substituted samples. A significant increase in optical bandgap with increasing of the Ce/Zr co-substitution suggests that the materials are suitable for technological applications. Magnetic properties of the samples show a magnetic transition from antiferromagnetic to ferromagnetic phase due to the presence of the rhombohedral to the tetragonal phase transition, and exchange interaction between the 4f orbitals of the Ce^{3+}/Ce^{4+} and the 3d orbitals of the Fe^{3+}/Fe^{2+}.

1 Introduction

$BiFeO_3$(BFO) is the most famous multiferroic material having the antiferromagnetic Néel temperature (= 370 K) and the ferroelectric Curie temperature (= 830 K) which simultaneously shows a saturation polarization and magnetic moment of 90 μC/cm^3 and 8–9 emu/cm^3, respectively [1]. The ferroelectricity and G-type antiferromagnetic characteristics of BFO come respectively from the lone-pair distortion on the $6s^2$ of Bi^{3+} ions and spin-exchange coupling between half-filled 'd' orbital of Fe^{3+} ions [2, 3].

Address correspondence to E-mail: gholizadeh@du.ac.ir; ah_gh1359@yahoo.com

https://doi.org/10.1007/s10854-021-07067-y
Published online: 25 September 2021

Despite this, inherent problems of the bulk BFO such as the formation of secondary phases, high leakage current, low magnetoelectric (ME) coupling, zero macroscopic remnant magnetization (M_r) have restricted its multifunctional applications at room temperature [4–7]. In recent years, attempts have been made to enhance reduce dielectric loss, ferroelectric properties, and leakage current, increase remnant polarization, modify its inhomogeneous-spatial spin-modulated (incommensurate) structure, and intensify magnetoelectric interaction [8–21]. However, comparative studies were undertaken to understand the effect of co-substitution at A- and B-site on ferroelectric and magnetic properties, respectively. Recent studies revealed that a strategy of co-doping of the Bi-site, and Fe-site can significantly improve the magnetic and ferroelectric properties of BFO nanoparticles, [11–19].

Arora et al. [20] reported successfully the substitution of Fe^{3+} with Zr^{4+} pure-phase Zr-substituted $BiFeO_3$ prepared with the hydrothermal method by several techniques. Our group recently reported that the A-site (Nd, Y, Gd) and B-site (Mn, Zr) co-substitution of BFO have a result to reduce the particle size to less than 62 nm which will destruct or suppress the magnetic spiral structure [6, 7]. However, in the present work, the hydrothermal method was used for the synthesis of pure single-phase $Bi_{1-x}Ce_xFe_{1-x}Zr_xO_3$ (x = 0.00, 0.03, 0.06) at a low temperature of 180 °C without a further calcination step. Since, $r_{Ce^{3+}}(CN:12) = 1.34Å$ is closer to the $r_{Bi^{3+}}(CN:12)(1.4$ Å, 6 s lone pair), the Ce substitution results in a low symmetry distorted rhombohedral structure with *R*3*c* space group accompanied by a large polarization along the hexagonal [001] or the pseudocubic [111] direction [21–23]. Furthermore, it highly expects that Bi^{3+}substitution with Ce^{3+} can reduce the leakage current density accompanied by a further improvement in the ferroelectric properties of BFO [23]. On the other side, the Ce^{4+} ions act as a donor because of their higher valance than that of Bi^{3+} ions, where the substitution of Ce^{4+} for Bi^{3+} requires charge compensation which can be achieved by the suppression of oxygen vacancies and Fe^{2+} [21]. the A-site Bi^{3+} ion of the BFO film shows a valence electron configuration of $6s^2$ $6p^0$; the lone $6s^2$ electrons of the Bi^{3+} ion hybridize with both the empty $6p^0$ orbits of the Bi^{3+} ion and the $2p^6$ electrons of the O^{2-} ion to form a Bi–O bond [24]. As for the Ce-substituted BFO film, the A-site Ce^{3+} and Ce^{4+} ions show valence electron configurations of $4f^1$ $5d^0$ $6s^0$ and $5p^6$ $4f^0$ $5d^0$ $6s^0$, respectively [25, 26]. The $4f^1$ electron of the Ce^{3+} ion hybridizes with the empty $5d^0$ and $6s^0$ orbits of the Ce^{3+} ion and the $2p^6$ electrons of the O^{2-} ion; meanwhile, the $5p^6$ electrons of the Ce^{4+} ion hybridize with the empty $4f^0$, $5d^0$, and $6s^0$ orbits of the Ce^{4+} ion and the $2p^6$ electrons of the O^{2-} ion to form Ce–O bonds, leading to a noncentrosymmetrically distorted structure and a suppressed spiral spin structure, probably improving the ferroelectric and magnetic properties of the Ce-substituted BFO. Previous reports on Zr^{4+} substitution for Fe^{3+} showed that lattice strains and defects originated from a mismatch in ionic radii prevent the growth of the grain sizes as the substitution increases and all the samples show the antiferromagnetic behavior [27]. While in A/Zr co-substitution for Bi/Fe, the particle sizes go down and a weak ferromagnetic behavior with an improvement of microwaves properties are observed [7, 28]. Detailed studies of structural, optical, and magnetic properties indicate novel behaviors of the pure single-phase $Bi_{1-x}Ce_xFe_{1-x}Zr_xO_3$ (x = 0.00, 0.03, 0.06) hydrothermally synthesized with improved magnetic properties.

2 Experimental

2.1 Preparation of $Bi_{1-x}Ce_xFe_{1-x}Zr_xO_3$

To prepare the $Bi_{1-x}Ce_xFe_{1-x}Zr_xO_3$ (x = 0.00, 0.03, 0.06) nanoparticles by hydrothermal method, first, a solution of initial material nitrates with appropriate moles under continuous stirring is obtained. The $Bi(NO_3)_3{\cdot}5H_2O$ is dissolved in 5 mL concentrated HNO_3 and then all $ZrO(NO_3)_2{\cdot}H_2O$, $Ce(NO_3)_3{\cdot}6H_2O$, and $Fe(NO_3)_3{\cdot}9H_2O$ were separately dissolved in 5 mL of distilled water. After that, all the precursors were mixed under continuous magnetic stirring to obtain a completely clear solution. Then, 40 g of KOH solution was dropwise added to the above solution and then the mixture was poured into a Teflon-lined stainless steel autoclave for the hydrothermal treatment at 180 °C for 6 h. The precipitate was filtered and washed with distilled water to remove $(NO_3)^{-1}$ and K^+ ions. Next, the resulted precipitate was dried in an oven at 110 °C for 3 h. To ensure accurate and reproducible results, the high

purity reagents and chemicals were used which were purchased from Sigma-Aldrich.

The crystal phase of the $Bi_{1-x}Ce_xFe_{1-x}Zr_xO_3$ (x = 0.00, 0.03, 0.06) nanoparticles was identified by powder X-ray diffraction (XRD, D8-Advance Bruker AXS diffractometer) with a Cu–Kα radiation (λ = 1.54048 Å). The patterns were analyzed using the Fullprof program [29]. Raman spectra were performed in a Renishaw 1000 confocal Raman microscope using a 532 nm diode-pumped solid-state laser (Cobolt) with a laser power of 10 mW. The Fourier transform infrared (FTIR) spectra of the samples were obtained from a Perkin–Elmer FT-IR spectrometer. The surface morphology images of the samples were recorded by field-emission scanning electron microscopy (FESEM, HITACHI S-4160 model) with the accelerating voltage of 10 kV. The absorption spectra of the samples were recorded by a UV–Vis system (Agilent8453, Palo Alto, CA). The direct-transition bandgap energy of the samples was estimated through Tauc's equation [30]. The hysteresis loops of the samples were recorded using the VSM 7407 Lake Shore's vibrating sample magnetometer at room temperature and a maximum magnetic field of 2 T.

3 Results and discussion

3.1 Structural analysis

Figure 1 shows XRD patterns of a single-phase perovskite structure of $Bi_{1-x}Ce_xFe_{1-x}Zr_xO_3$ (x = 0.00, 0.03, 0.06) nanoparticles. It reveals the presence of a rhombohedral crystal structure with $R3c$ space group for BFO which is in accordance with the JCPDS card (no. 86-1518) [7]. After Ce^{3+}/Zr^{4+} ions doping into BFO, the doublet diffraction peaks (104) and (110), (006) and (202), (116) and (112), (118) and (300) of the rhombohedral structure are merging to the singlet peak as shown in Fig. 1. Also, the location of all the diffraction peaks shifted toward a higher angle.

Although the intensity of XRD peaks located at the higher angles is increasing, the intensity of singlet peak $(012)_R$ at about 22° becomes smaller. Besides, an enlarged view of $(012)_R$ and $(024)_R$ reflections is plotted inset of Fig. 1 to show the structural change as Ce^{3+}/Zr^{4+} content increases up to x = 0.06. As seen from Fig. 1, a splitting in both the parallel $(012)_R$ and $(024)_R$ reflections of the rhombohedral structure which are singlet peaks, occur with the addition of

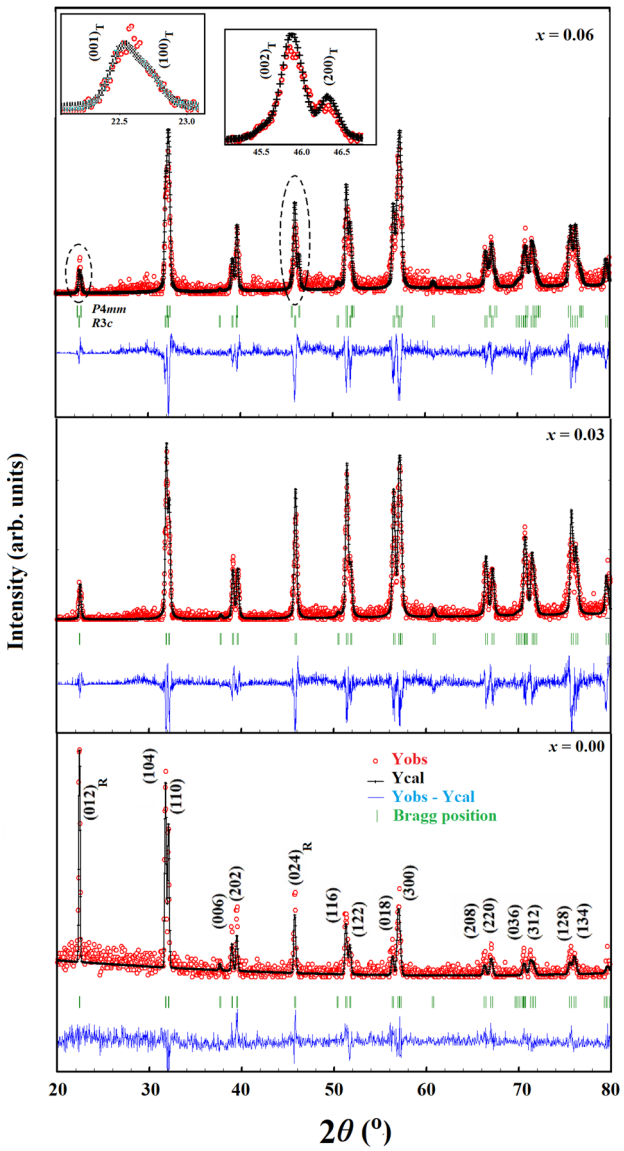

Fig. 1 XRD pattern and Rietveld analysis with rhombohedral (space group $R3c$) structural model for $Bi_{1-x}Ce_xFe_{1-x}Zr_xO_3$ (x = 0.00, 0.03) and a mixed-phase tetragonal ($P4mm$) + rhombohedral ($R3c$) structural models for x = 0.06. Red circles and black solid lines represent the raw data and the calculated profile, respectively. Green vertical lines indicate the position of Bragg peaks for rhombohedral structure. The blue lower trace shows the difference between the observed (the raw data) and the calculated patterns (Color figure online)

Ce^{3+}/Zr^{4+} content. The singlet $(012)_R$ peak is split into two sub-peaks, a larger peak at about 22.50° and a smaller peak at about 22.75° which are respectively corresponded to the reflection planes $(001)_T$ and $(100)_T$ of tetragonal structure. Similarly, the singlet $(024)_R$ peak is split into two sub-peaks, a larger peak at about 45.90° and a smaller peak at about 46.40°

which are respectively corresponded to the reflection planes $(002)_T$ and $(200)_T$ of the tetragonal structure. It should be noted that the intensity of the $(001)_T$ and $(002)_T$ reflections of the tetragonal structure is smaller than the $(100)_T$ and $(200)_T$, respectively [31]. Since the structure of sample $x = 0.06$ is a mixture of the tetragonal ($P4mm$) and rhombohedral ($R3c$) phases, the peak overlap of the $(012)_R$ with the $(001)_T$ and the peak overlap of the $(024)_R$ with the $(002)_T$ occurs. These findings could be related to the fact that the lower symmetry rhombohedral structure of BFO gradually transforms into a higher symmetry tetragonal structure due to the changes of bond lengths Bi–O and Fe–O after the Ce^{3+}/Zr^{4+} doping into BFO, which is discussed further below.

The Rietveld refinement of the XRD patterns of the samples using Fullprof software confirms the formation of the rhombohedral structure with $R3c$ space group (see Fig. 1). The refined lattice parameters and error bars of parameters in parentheses, as well as R-factors values related to the quality of Rietveld refinement (R_p, R_{wp}, R_{exp}) and χ^2 (goodness of fitting), are listed in Table 1. The difference between observed and calculated curves can be due to noisy data observed over the whole angle range which results in the high values of R factors (R_p, R_{wp}, R_{exp}), while χ^2 value shows the best goodness of fitting. Generally, the major factors causing a noisy XRD pattern are poorly crystalline sample, the measurement conditions, Cu–Kα X-rays.

The factor of the poorly crystalline sample is related to the amorphous sample having an XRD pattern with broad and low-intensity peaks. However, the height of XRD peaks in our samples is very high compared to the noisy background. If there is an impurity phase of ZrO_2 or CeO_2 in the samples, it needs to be at least the preferred peaks belonged to the impurity phases of ZrO_2 or CeO_2 in the XRD pattern of our samples. However, there are no preferred peaks from oxides ZrO_2 and CeO_2 in our samples. Also, the presence of a potassium line in the EDS spectrum of all the samples can suggest the formation of a small impurity phase containing K element (already, we cannot find any trace) which may be contributed to the noise background. As can be seen, all the Raman peaks were been completely belonged to BFO rhombohedral structure with no trace of the Raman peak of the impurity phase containing the K, Zr, or Ce elements. It should be noted that previous reports showed successfully the substitution of Bi^{3+}/Fe^{3+} with Ce^{3+}/Zr^{4+} into $BiFeO_3$ [7, 13, 21, 24–28, 32–34]. Also, the successful synthesis of pure-phase $BiFeO_3$ and Zr-substituted $BiFeO_3$ prepared with hydrothermal method were investigated by several techniques [20, 35].

The sample fluoresces is most pronounced when the source Cu–Kα radiation energy is only slightly greater than the characteristic X-rays of the sample (that are rich in Fe, Cr, Mn). In Cu diffractometer, the energy of the Cu–Kα (1.54 Å) is sufficiently high to excite the Fe atoms (which conjointly stimulates the

Table 1 The lattice parameters of conventional hexagonal (a_H, c_H), primitive rhombohedral (a_R, α_R) structures, the crystallite size ($D_{W\text{-}H}$) and microstrain (ε) obtained from the Williamson-Hall method for $Bi_{1-x}Ce_xFe_{1-x}Zr_xO_3$ with their error bars in parentheses and R-factors values related to the quality of Rietveld refinement (R_p, R_{wp}, R_{exp},) and χ^2 (goodness of fitting)

Sample	$x = 0.03$	$x = 0.00$	$x = 0.06$	
			Rhombohedral	Tetragonal
$a_H = b_H$ (Å)	5.584 (9)	5.569 (1)	5.569 (1)	3.919 (3)
c_H (Å)	13.87 (9)	13.83 (8)	13.82 (5)	3.983 (2)
$a_R = b_R = c_R$ (Å)	5.639 (4)	5.622 (8)	5.618 (5)	–
$\alpha_R = \beta_R = \gamma_R$ (°)	59.36 (0)	59.36 (9)	59.39 (1)	90
$V_R = V_H/3$ (Å^3)	124.9 (7)	123.9 (0)	123.6 (7)	61.18 (5)
$D_{W\text{–}H}$ (nm)	82.2 (7)	28.7 (8)	28.7 (8)	
ε (no unit)	+ 11.3(0)E−4	− 5.31 (5)E−4	− 5.31 (8)E−4	
Rietveld R factors				
R_p	68.7	40.3	52.4	
R_{wp}	64.4	49.7	56.8	
R_{wp}	55.9	36.1	40.7	
χ^2	1.32	1.89	1.94	

FeKα (1.94 Å) line and consequently engenders X-ray fluorescence) and the Fe-rich samples will fluoresce under the incident Cu–Kα beam which creates a combination of both Cu–Kα and Fe radiations with different wavelengths plus the continuum radiation entering the detector. It can lead to strange shaped and elevated backgrounds causing a noisy XRD pattern. Since the sample $x = 0.06$ contains more Fe than sample $x = 0.00$, the diffraction patterns of the sample $x = 0.06$ tend to feature a greater background. Potential resolutions of this issue are to utilize Co–Kα radiation (1.79 Å) or to shield the front of the detector with a PVC filter, which will absorb the low energy fluorescence. Sometimes the noise/signal ratio can be reduced by going to lower scan rates or by opening up the slit size to allow a greater X-ray flux. Finally, the feature of noisy data observed in XRD patterns of all the samples over the whole angle range was due to the low-qualified measurement system which results in the high values of R factors (R_P, R_{wp}, R_{exp}).

The hexagonal cell is no longer primitive and has three times the volume of the rhombohedral cell. When the XRD pattern of a rhombohedral sample is indexed, i.e., with reference to hexagonal axes and the true nature of the lattice determined, we usually want to know the lattice parameters a_R and α_R of the rhombohedral unit cell. But the dimensions of the rhombohedral cell can be determined from the dimensions of the hexagonal cell and this is an easier process than solving the rather complicated plane-spacing equation for the rhombohedral system. The first step is to analyze and index the XRD pattern based on the hexagonal axes using the Fullprof program. Then, the parameters a_H and c_H of the hexagonal cell are calculated in the usual way. Finally, the parameters a_r and α_R of the rhombohedral cell are determined from the refined parameters a_H and c_H of the hexagonal cell using the Fullprof program [6].

Primitive rhombohedral and hexagonal structures in a stable perovskite structure of $BiFeO_3$ are shown in Fig. 2. The values of the ion radius of the cations used in this work which are located at the sixfold coordination site (octahedron site) and the 12-fold coordination site (dodecahedral site), are as follow:$r_{Ce^{3+}}(CN:12) = 1.34Å$, $r_{Ce^{4+}}(CN:12) = 1.14Å$, $r_{Bi^{3+}}(CN:12) = 1.4Å$, $r_{Fe^{3+}}(CN:6) = 0.645Å$, $r_{Zr^{4+}}(CN:6) = 0.72Å$ [36, 37]. According to these values, substituting the smaller Ce^{3+} for larger Bi^{3+}, will reduce the unit cell volume. Simultaneously, it is expected that Zr^{4+} replacement instead of Fe^{3+} will increase the unit cell volume. For better discussion, we calculated the difference in ion radii of the host ions with the substituted ions as follows:

$$r_{Ce^{3+}} - r_{Bi^{3+}} = -0.06Å, \quad r_{Zr^{4+}} - r_{Fe^{3+}} = +0.075Å$$

Therefore, it is expected that the lattice volume will increase with the Ce^{3+}/Zr^{4+} co-substitution in BFO. However, a shift of the XRD peaks to the larger angles with an accompanying decrease of the lattice volume suggests the presence of various cations of $Ce^{3+}$and Ce^{4+} in the samples (see Table 1). It should be noted that it is harder to enter the Zr^{4+} ions having an ionic radius larger than Fe^{3+}, which may results in the oxidation of Ce^{3+} to Ce^{4+}. Since the electronic configuration of Ce is $4f^1\ 5d^1\ 6s^2$ (atomic number of 58), one among the lanthanides, Ce^{3+} ions having the configuration $4f^1\ 5d^0\ 6s^0$ can easily lose an electron to acquire the configuration $4f^0$ and attains the stable configuration of Xenon. The Ce has two stable valence states, + 3 and + 4 indicating that Ce^{4+} ion substituting Bi^{3+} ion plays a role of a donor in the oxygen octahedron because of its higher valance than that of Bi^{3+} ions, charge compensation which can be achieved by the suppression of the inherent oxygen vacancy concentration, thus resulting in the restrained reduction of Fe^{3+} to Fe^{2+} [24]. Since the ionic radii of Ce^{4+} ions are smaller than that of Bi^{3+} ions, and the valence of Ce^{4+} ions is higher than that of Bi ions, the substitution of Ce^{4+} for Bi^{3+} may induce structural distortion (or even structural transition) and change local electron density in the lattice [25].

The increase in the angle of α_R near to 60° and decreasing of the lattice parameters given in Table 1 with the doping amount of $(Ce^{3+}–Ce^{4+})/Zr^{4+}$ ions indicates a slight contraction of the FeO_6 octahedral along the body diagonal [111] of rhombohedral (111) axis (c axis of hexagonal) or the c-axis [001], which is accompanied with a transition to a higher symmetry structure (see Fig. 2) [6, 7].

In the Williamson–Hall (W–H) method (Fig. 3), the $\beta\cos\theta$ (y-axis) plot versus $4\sin\theta$ (x-axis) corresponding to the three parallel reflection planes (012), (024), (036) has a positive slope for BFO, while it indicates a negative slope for Ce/Zr co-substituted BFO. The crystallite size (D) is calculated by the inverse of the y-intercept of linearly fitted data and microstrain (ε) is obtained from the slope [38]. The results of Table 1

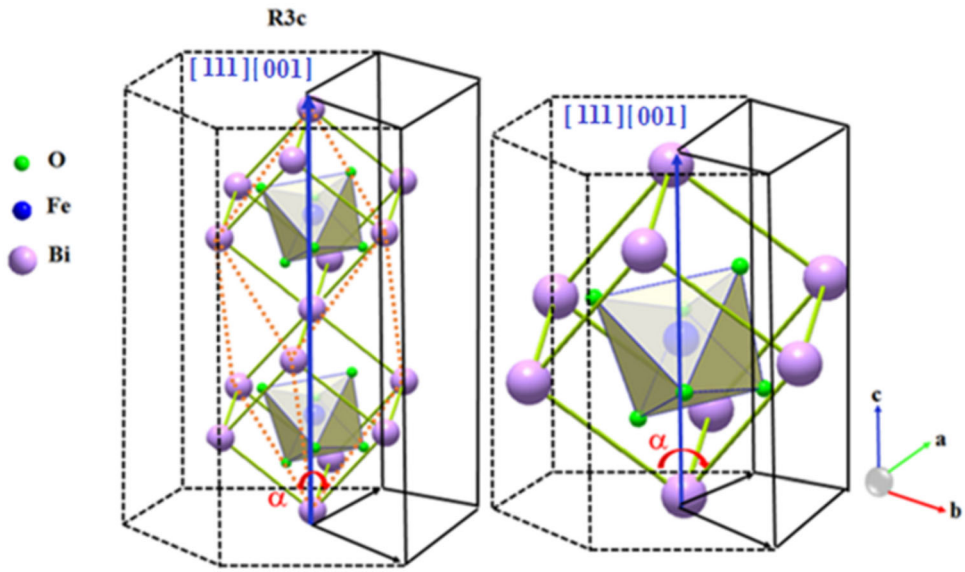

Fig. 2 Left panel is a scheme of the relationship between the primitive rhombohedral (dashed, red), cubic (solid, green), and hexagonal cells of bulk BFO. The right panel is half of the left panel. Here, [001] crystallographic axis of the hexagonal structure is parallel to the [111] axis of the rhombohedral or the cubic structures (Color figure online)

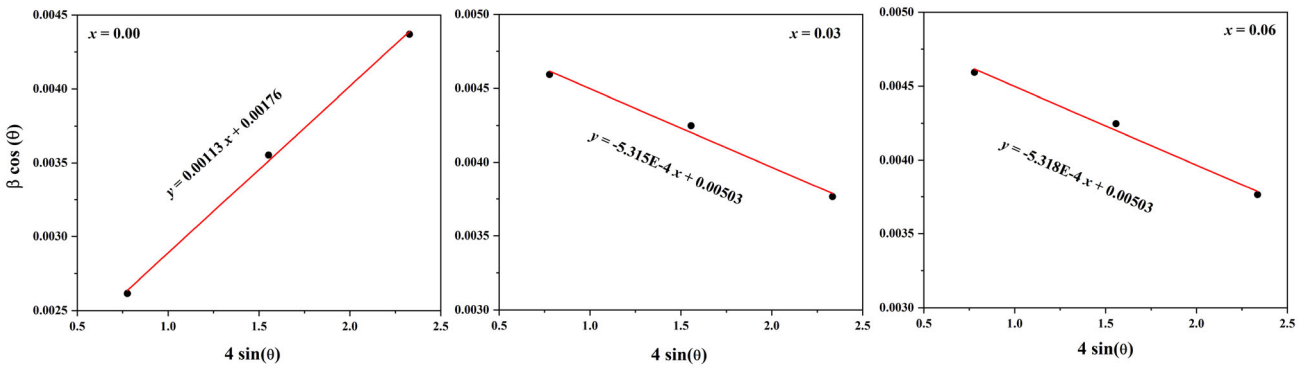

Fig. 3 Williamson-Hall plots of $Bi_{1-x}Ce_xFe_{1-x}Zr_xO_3$

show the remarkable changes in the crystallite size and the microstrain contribution from the broaden X-ray profile for the Ce/Zr co-substituted BFO. With the increase of the Ce/Zr co-substitution in BFO, the value of the D decrease and the ε become negative due to the presence of compressive stress. This compressive stress created into the BFO lattice can be related to the following reasons: First, ionic radii mismatch between Ce^{3+}/Ce^{4+} and Zr^{4+} ions with the Bi^{3+} and Fe^{3+}, respectively, causes the stresses and defects in the lattice of BFO that prevent further the growth of the crystallite sizes [28, 29]. Second, the evaporation of Bi for sintering the BFO at 750 °C induces vacancies due to the low melting point of Bi (271 °C). By increasing the replacement of rare-earth ions such as Ce (795 °C) instead of Bi, the oxygen vacancies will be reduced, which prevents the migration of the oxygen ions between the particles and thus the decrease in growth and the size of the crystallites or nanoparticles [5]. Third, since the Zr–O bond is stronger than the Fe–O bond, substituting the nonmagnetic Zr^{4+} ion for Fe^{3+} in BFO leads to a decrease in the concentration of the oxygen vacancies. This prevents the formation of oxygen vacancies and slows down their motion between particles, which results in a reduction in the crystallite size by increasing the Zr^{4+} substitution [24].

3.2 Raman and FTIR spectroscopies

Many reasons are indicating that the local structure analysis of substituted BFO nanoparticles can be explained more clearly by the IR and Raman spectroscopies: (1) The structural analysis of BFO nanoparticles by XRD is hampered by the reflection broadening so that splitting the XRD peaks of BFO just covered by the broadening [6]. (2) In particular,

the presence of Fe in combination with Cu-$K\alpha$ radiation leads to significant X-ray fluorescence and high measured backgrounds [38]. These easily can cover the presence of low-level impurities.

Figure 4a shows the Raman spectra measured at room temperature for $Bi_{1-x}Ce_xFe_{1-x}Zr_xO_3$. According to group theory, distorted rhombohedral $BiFeO_3$ have 18 optical vibration modes (= 4A1 + 5A2 + 9E), which A1 (TO) and E (LO) are Raman and infrared active vibration modes, respectively, and 5A2 are Raman inactive vibration modes. So, the 13-point Raman active phonons (= 4*A*1 + 9*E*) of distorted rhombohedral perovskite structure (*R*3*c* space group) can propagate in longitudinal and transverse directions as following [39]: Four *A*1 modes propagating along the c-direction, *A*1–1, *A*1–2, *A*1–3, and *A*1–4 and nine E modes propagating along the *x*–*y* plane. Generally, the *A*1–1 and *A*1–2 modes show strong scattering intensities, whereas the *A*1–3, and *A*1–4 modes show weak scattering intensities [32, 35, 40–43]. By comparison, the scattering intensity of nine E modes is medium. However, the resonance frequency and the shape of the spectral line depend on the characteristics of the samples. According to previous reports [35, 40–42], the polar phonon modes of *A*1–1, *A*1–2, and E1 are mainly contributed to spin-phonon coupling, magnetic anisotropy, and magnetoelectric coupling, respectively. In this research, a slight shift of the *A*1–1, *A*1–2, and *A*1–3 modes (assigned to the Bi–O bonds) to higher frequencies and a significant change in their intensities with the increase of the Ce and Zr co-substitution indicate that the Ce^{4+} ions of smaller size are substituted for the Bi^{3+} ions. Figure 5 shows two strong peaks near 132, and 168 cm^{-1} assigned to the *A*1–1, and *A*1–2 phonon modes and two weak peaks at 224, and 426 cm^{-1} assigned to *A*1–3, and *A*1–4 phonon modes. Also, the Raman spectra indicate a significant decrease in the scattering intensity of *A*1–1 mode and an obvious increase in the scattering intensity of *A*1–2

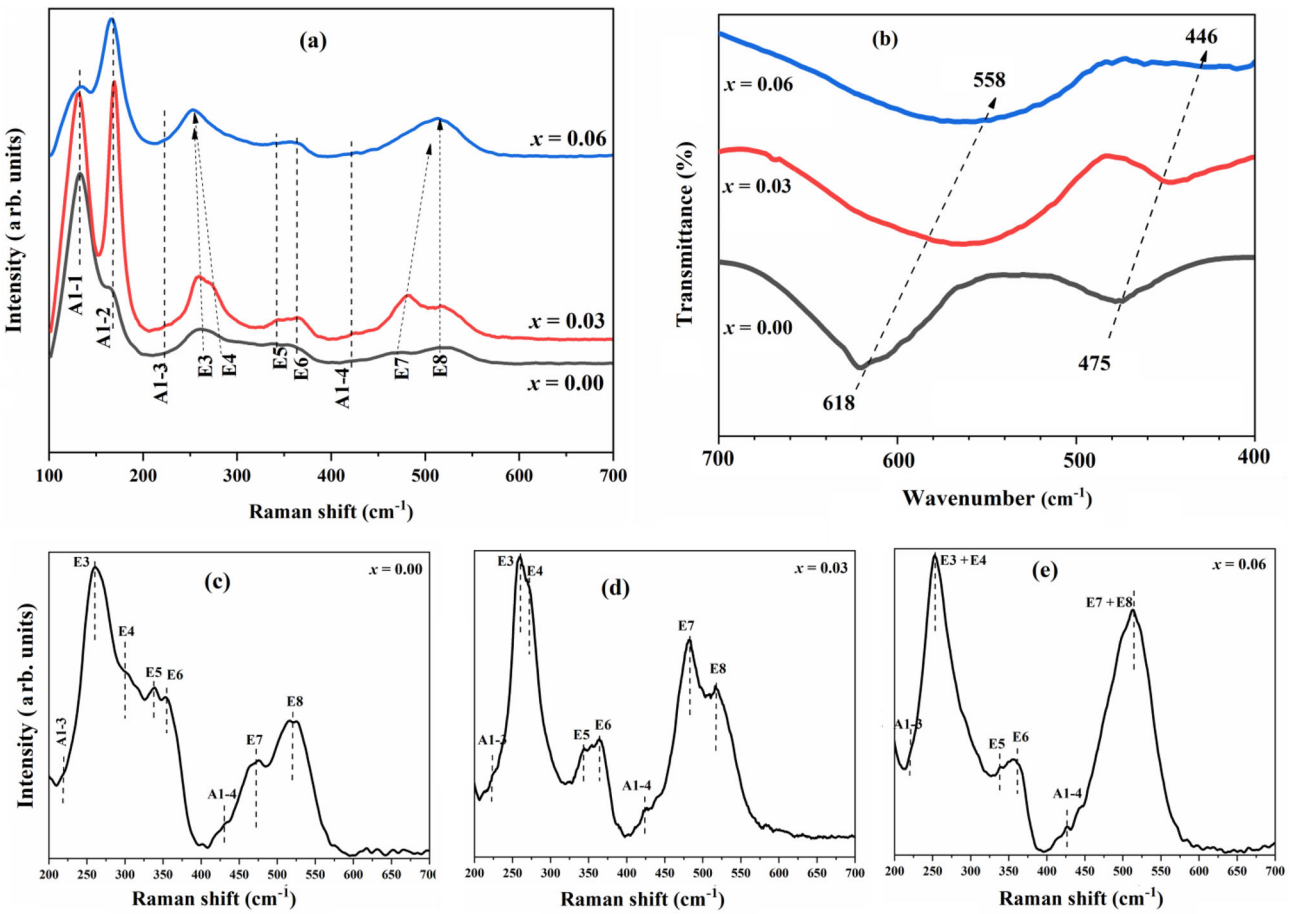

Fig. 4 **a** Raman spectra, **b** normalized FT-IR spectra of $Bi_{1-x}Ce_xFe_{1-x}Zr_xO_3$. Selected enlarged raman region (200–700 cm^{-1}) of samples, **c** $x = 0.00$, **d** $x = 0.03$, **e** $x = 0.06$

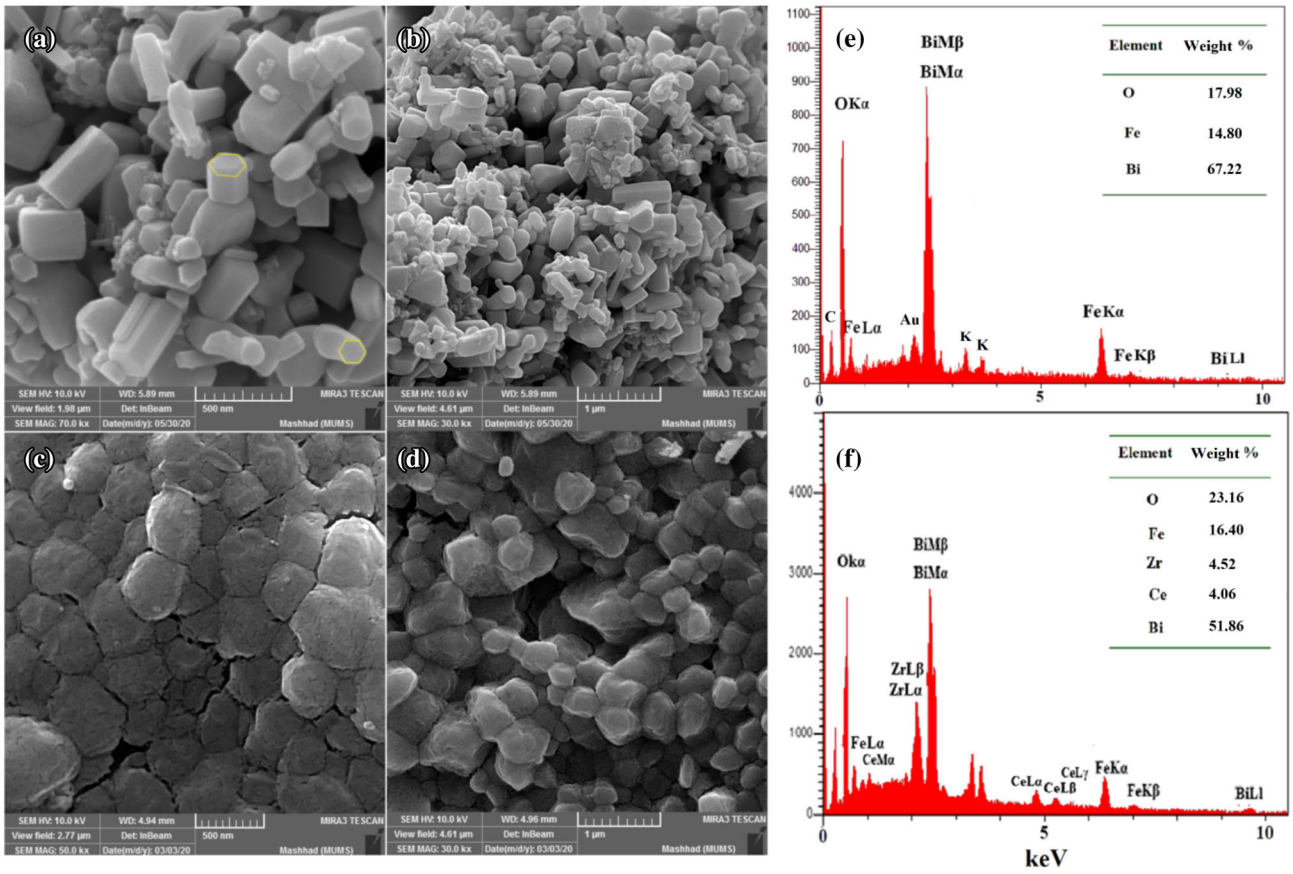

Fig. 5 FE-SEM images for **a**, **b** $x = 0.00$, and **c**, **d** $x = 0.06$ on a scale of 500 nm and 1 μm, respectively. EDS analysis of **e** $x = 0.00$, and **f** $x = 0.06$. The spectral lines of the undesirable elements (K, C and Au) are shown on (**e**)

mode as the Ce/Zr co-substitution increase. The relatively reduced intensity of the $A1$–1 mode with the degree of the Ce/Zr co-substitution indicates a decrease in the spin-phonon coupling. The relatively enhanced intensity of $A1$–2 Raman mode with increasing the Ce/Zr co-substitution in BFO indicates that two predominant scattering mechanisms controlling the magnetic anisotropy are the spin-dependent and spin-phonon scattering, so that the Raman intensity of a magnetically ordered phase can be expressed as $I = \left|R + M\langle S_i S_j\rangle/S^2\right|^2$. Here, R and M are the spin-independent, and the magnetic moment parameters, respectively, and $S_i S_j/S^2$ is the nearest-neighbor spin–spin correlation function. The increase in the intensity of A1–2 mode is due to different contributions from the correlation function $S_i S_j/S^2$, in different directions, which is the result of a change in the magnetic ordering due to the spin-reorientation phase transitions. According to our structural results, it may be attributed to the presence of $(001)_T$ and $(002)_T$ peaks oriented in the c-axis direction of the Ce/Zr co-substituted BFO.

The positions of all the observed Raman peaks for samples $Bi_{1-x}Ce_xFe_{1-x}Zr_xO_3$ are given in Table 2. The atomic mass also plays a very important role in a

Table 2 Raman peak positions for samples $Bi_{1-x}Ce_xFe_{1-x}Zr_xO_3$

Raman modes (cm^{-1})	$x = 0.00$	$x = 0.03$	$x = 0.06$
A1-1	132	136	136
A1-2	163	167	169
A1-3	218	224	223
A1-4	428	428	428
E3	260	259	252
E4	299	270	256
E5	337	341	341
E6	353	363	363
E7	471	482	513
E8	518	518	518

The unit is cm^{-1}

harmonic vibrating system ($\omega = \sqrt{K/m}$). The molar mass of Fe^{3+}, Zr^{+4}, Bi^{3+}, Ce^{3+}, and Ce^{4+}, are 55.845, 91.22, 208.979, 140.114, and 139.905 g/mol, respectively. The molar masses of the Ce^{3+} and Ce^{4+} are less than that of the Bi^{3+}. Nevertheless, at a replacement of less than 15%, the calculated average molar mass does not have much effect [40].

The Raman spectra (Fig. 4c–d) show remarkable changes in some band shifts, the expansion of the line-width of all bands, and the weakening in the intensity of the BFO structure with the increases of Ce/Zr content. It indicates an intensity change in *A*1 modes and the shift in the *E* modes. As seen, the intensity of the *A*1–1 mode decreases, while *A*1–2 phonons increases after Ce/Zr ions are incorporated. When Ce/Zr co-substitution increases up to 0.06, *E*4 mode at 299 cm^{-1} shifts to a lower wavenumber, followed by merging with the phonon mode *E*3 at 263 cm^{-1}. At the same time, the *E*7 mode at 471 cm^{-1} shifts to a higher wavenumber, followed by merging with the phonon mode *E*8 at 518 cm^{-1}. According to our structural results, an increase in the intensity of the *E*7 mode may be attributed to the presence of peaks $(100)_T$ and $(200)_T$ oriented in an *a*-axis direction in the Ce/Zr co-substituted BFO. Also, the *E*5 and *E*6 modes at 343 and 367 cm^{-1}, respectively, become gradually weak and finally disappear. On the other hand, the mean radius of the Ce^{3+}/Ce^{4+} ions is smaller than that of the Bi^{3+} ions, which a decrease in *d* spacing yields a compressive force into the A-sites of the BFO lattice as seen from Fig. 3. As seen from our structural analysis given in Table 1, it suggests an incomplete structural transition from a rhombohedral structure to a higher symmetry pseudo-tetragonal by Ce/Zr substitution up to $x = 0.06$. which its structure is a mixture of rhombohedral and tetragonal phases. When the induced microstrain by the Ce/Zr co-substitution causes the BFO structure to transits to tetragonal (*P*4*mm* space group), the Raman active modes can be expressed by the following irreducible representation: $3A1 + B1 + 4E$ [43].

Figure 4b shows normalized FT-IR spectrum of $Bi_{1-x}Ce_xFe_{1-x}Zr_xO_3$ ($x = 0.00$, 0.03, 0.06). It is known that the absorption frequencies observed in the range of 400 to 700 cm^{-1} are related to metal–oxygen vibrations of the perovskite structure [44–46]. The strong absorption frequencies found at wavenumbers 475 and 618 cm^{-1} of the BFO are related to the asymmetric bending and the symmetric stretching vibrations of the iron–oxygen bond in the FeO_6 octahedral iron sites. The former frequency only appears in the high-distortion rhombohedral structure of the perovskite oxides [32]. As seen from Fig. 4b, there is no absorption peak at about 446 cm^{-1} for $x = 0.06$, indicating a structural phase transition from *R*3*c* low symmetry rhombohedral structure to *P*4*mm* high-symmetry tetragonal structure occurs as obtained from XRD and Raman analysis. However, we can observe that the position of absorption peak located at 618 cm^{-1} shifts to a lower wavenumber located at 558 cm^{-1}, indicating successful substitution of the Fe^{3+} ion by a bigger Zr^{4+} ion.

3.3 Morphological analysis

Figure 5 shows FESEM images for the $Bi_{1-x}Ce_x$-$Fe_{1-x}Zr_xO_3$ ($x = 0.00$, 0.06) on a scale of 500 nm and 1 μm. It is seen that the morphology of BFO (Fig. 5a, b) is completely different from the morphology of Ce/Zr co-substituted BFO (Fig. 5c, d). As the concentration in the substitution increases, the elongated polyhedral and hexagonal grains cease to exist, and granular structures of rounded shape emerge. This result suggests the presence of two different structural phases in accordance with the rhombohedral-to-tetragonal structural phase transition observed by the structural results. In addition, the observed micro- and nano-size grains of BFO has a hexagonal basal plane with a nonhomogeneous distribution. It is clear that Ce/Zr co-substitution increases the grain size and the platelet hexagons show lower porosity and higher density than that for BFO. According to the structure results, further reduction in the internal microstrain with increasing the Ce/Zr co-substitution accompanied by a reduction in internal energy and pressure can only be achieved by a decrease of the grain boundary or increase of the grain size [7]. An X-ray energy-dispersive spectroscopy (EDS) connected to the FE-SEM was used for the elemental analysis of the samples $x = 0.00$ and $x = 0.06$ as shown in Fig. 5e and f, respectively. In the spectra, the energy lines are observed for composition elements Bi, Ce, Zr, Fe, and O. The obtained values of weight percentages of each of the elements are listed in the inset of Fig. 5e and f for samples $x = 0.00$, 0.06. The spectral lines of the undesirable elements (K, C, and Au) in EDS analysis are shown in Fig. 5e. Au line has an overlap with the Zr line that can increase uncertainty in the concentration of the Zr element.

However, our non-conducting specimens for SEM should be coated with a conductive material such as Au which is one of the most common coatings. The presence of K lines in EDS spectra of the samples shows that the washing process of the samples with water was not enough to remove $(NO_3)^{-1}$ and K^+ ions.

The uncertainty in the concentrations can vary over a wide range, and large uncertainties are usually observed when the concentration of an element is low. Also, large uncertainties are expected when the sample contains elements with large differences in the Z number (such as oxygen, carbon, and significantly heavier metals). One can realize such large uncertainties by repeating measurements at the same spot of the sample. The background profile and overlap of a given spectral line may affect the results significantly. The best results can be obtained when the spectral line of the element does not overlap with other lines, and when the background is fitted accurately and subtracted from the spectral area. Also, lower uncertainty is expected from high-intensity spectra (obtained by long acquisition times). Above discussion suggest that EDS analysis shows a few percentages error in major concentration elements but up to several ten percentages error in minor or trace elements.

The values of weight percentages of composition elements for $x = 0.00$ are 67.22% Bi, 14.80% Fe and 17.98% O and for $x = 0.06$ are 51.86% Bi, 4.06% Ce, 16.40% Fe, 4.52% Zr and 23.16% O. However, from uncertainty in the concentrations originated from the errors as discussed above, we can conclude that there is a relative good agreement between these weight percentages and those expected from the formula, according to which for $x = 0.00$, 66.8% Bi, 17.85% Fe and 15.35% O are expected, while for $x = 0.06$, 63.29% Bi, 2.57% Ce, 16.91% Fe, 1.76% Zr and 15.46% O are expected.

3.4 Optical characterization

Figure 6a–c show Tauc plots of $(\alpha h\upsilon)^2$ versus the photon energy ($h\upsilon$) of $Bi_{1-x}Ce_xFe_{1-x}Zr_xO_3$ ($x = 0.00$, 0.03, 0.06). The direct energy gap has been calculated from the extrapolating of the linear part of the plots, as shown in Fig. 6a–c. The bandgap determination is based on a linear fit of the curve $(\alpha h\upsilon)^2$ vs. $h\upsilon$ (between 3.0 and 3.75 eV) using OriginPro software. We can assume that $(\alpha h\upsilon)^2 = 0$ (intercept of $h\upsilon$-axis), and

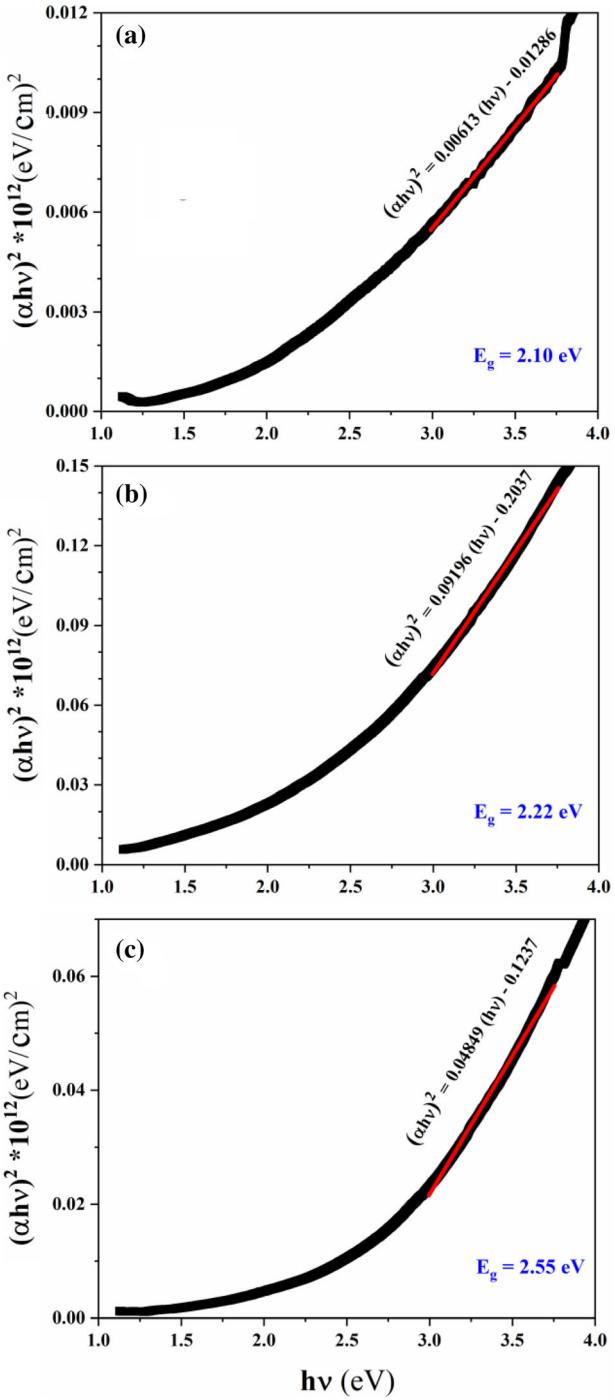

Fig. 6 Plots of $(\alpha h\upsilon)^2$ versus $h\upsilon$ for samples **a** $x = 0.00$, **b** $x = 0.03$, **c** $x = 0.06$

can therefore rearrange the equation $(\alpha h\upsilon)^2 = mh\upsilon + c$ to $h\upsilon = E_g = -c/m$. The standard errors of the components (slope, intercept) of the linear fit determine the overall error of the measured bandgap. The bandgap energy of BFO (= 2.10 eV) is related to

the electronic charge transfer from O 2p states (valence band) to Fe-3d states (conduction band) which were increased with Ce/Zr co-substitution up to 2.55 eV for $x = 0.06$.

Zhou et al. [47] have reported an increase in optical bandgap in Sm and Mn co-doped BFO which may be due to Burstein–Moss effect. A similar increase in optical bandgap is also reported for Y and Co co-doping of BFO due to a decrease in the density of state in the valence band [48]. However, there are contradictory reports on the effect of Ce substitution on the bandgap energy of BFO [33, 34, 49]. Here, the increase of the gap energy cannot be originated from the quantum confinement phenomenon (see the SEM images). It can be attributed to the following reasons: (1) the synergetic effect of Ce and Zr co-substitution on the band structure of BFO is due to the change of the Fe–O and the Bi–O length bonds and the Fe–O–Fe bond angles which may cause a decrease in the density of state in the valence band. (2) According to Burstein–Moss effect, some states close to the conduction band being populated would result in a blue shift of the optical bandgap, with increasing Ce content (Ce acts as a donor) [7, 24, 33, 34, 47, 48]. These will lead to a shift in the fundamental absorption edge towards higher photon energy. A significant increase in optical bandgap energy with increasing of the Ce/Zr co-substitution suggests that the materials are suitable as UV and blue–green-driven photocatalysts, or for optoelectronic devices.

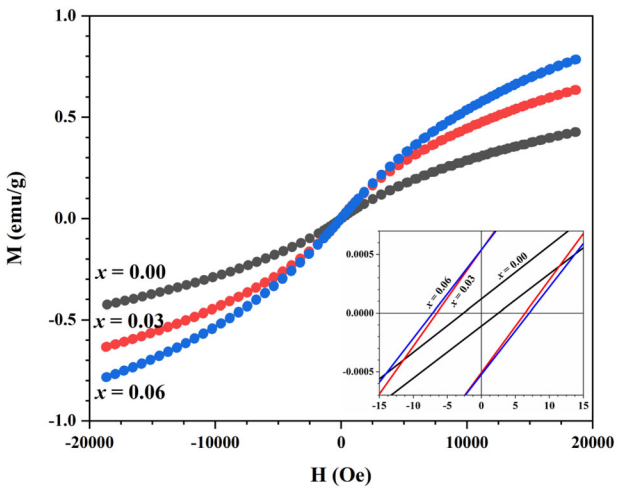

Fig. 7 Magnetization curve measured at 300 K for $Bi_{1-x}Ce_xFe_{1-x}Zr_xO_3$ (Inset: the enlarged view of the magnetization at the low magnetic field)

3.5 Magnetic measurements

The room temperature magnetization curves of $Bi_{1-x}Ce_xFe_{1-x}Zr_xO_3$ ($x = 0.00, 0.03, 0.06$) are shown in Fig. 7. From the curves, we can extract the highest field magnetization (M_H), coercive field (H_c), magnetization at zero applied fields (M_r, the remanent magnetization) for the samples as listed in Table 3.

According to the law of approach to saturation (LAS), anisotropy constant can be calculated by fitting the magnetization curves at the high sufficiently field regions ($H \gg Hc$) with relation (see Fig. 8): $M(H) = M_s(1 - a/H - b/H^2) + \chi H$, where $M(H)$ is the magnetization at the applied field H [49–51]. Also, the parameters M_s, a, b, and χ are saturation magnetization, inhomogeneity parameter, factor proportional K_1^2 (K_1 anisotropy constant), and susceptibility, respectively. They are obtained from the fitting method and listed in Table 3. According to our structural results, the Fe^{3+} ion extracts an electron from Ce^{3+} to form Ce^{4+} and Fe^{2+} ions. However, the Fe^{2+} ion contributes to anisotropy, but the Fe^{3+} ion is expected to be isotropic based on its electron structure. Finally, the increase in the coercive field in Ce/Zr-substituted samples with the substitution has been attributed to the increase of the Fe^{2+}/Fe^{3+} ratio and K_1 anisotropy constant.

An almost linear increase and small values of the magnetization curves indicate the antiferromagnetic nature of sample BFO which is changed to the weak ferromagnetic as Ce/Zr co-substitution increase (see Fig. 8). However, the presence of the paramagnetic nanoparticles or high magnetic anisotropy of the samples causes the magnetization curves to do not saturate even in the highest applied fields [7, 51]. The increase of M_r and M_H with the Ce/Zr substitution can be related to three reasons: First, a mixture of the rhombohedral and tetragonal structural phases can destroy the spiral spin modulation with an increase of the magnetization [6, 7, 52, 53]. Second, when magnetic ion Ce^{3+} having a large magnetic moment of 2.4 μ_B substitutes for nonmagnetic ion Bi^{3+}, an exchange interaction between 3d orbital of Fe^{3+} ion and 4f orbital of Ce^{3+} ion at the B- and A-sites, respectively, produce a local ferrimagnetic spin configuration accompanied by a magnetic enhancement [54]. Third, it is known that the reduction in the particle size of BFO below 62 nm (the period length of the spiral spin structure in bulk BFO) destroys the

Table 3 The values of remanent magnetization (M_r), coercivity (H_c), and magnetization at the highest applied field (M_H) and the fitting parameters of LAS curve ($M = M_s(1 - a/H - b/H^2) + \chi H$) for $Bi_{1-x}Ce_xFe_{1-x}Zr_xO_3$

Sample	H_c (Oe)	M_H (emu/g) at 2 T	M_r (emu/g)	a (Oe)	$b*10^{-6}$ (Oe^2)	$\chi*10^5$ (emu/Oe)
$x = 0.00$	2.56	0.427	0.96E−4	2975.78	2.93	1.38
$x = 0.03$	6.50	0.634	5.23E−4	2738.87	2.62	1.86
$x = 0.06$	7.10	0.784	5.31E−4	3154.20	3.18	2.41

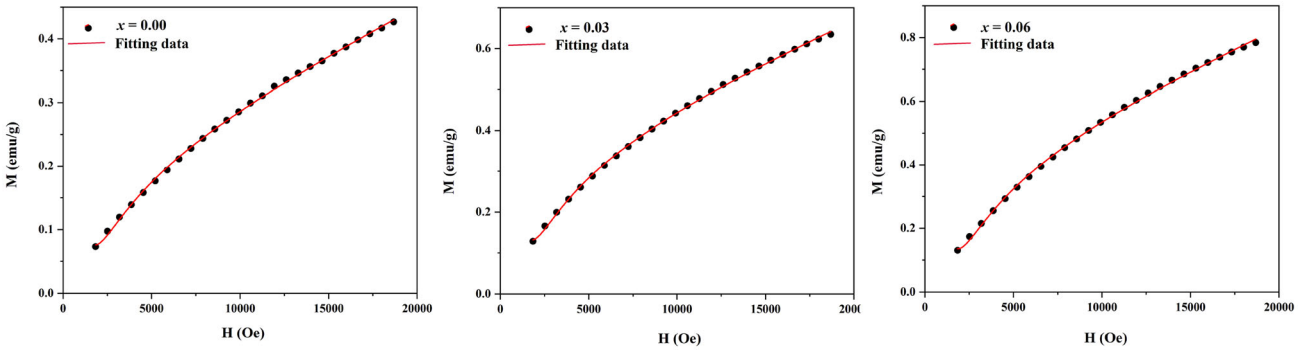

Fig. 8 LAS curves for $Bi_{1-x}Ce_xFe_{1-x}Zr_xO_3$

periodicity of the spin cycloid which makes the ferromagnetic order prevail over the antiferromagnetic order [7, 51]. Furthermore, the larger ratio of the surface to the volume and mismatch in the ionic radii increases the uncompensated surface spins at the surface of nanoparticles, which can play a significant role in the enhancement of the particle's overall magnetization of the Ce/Zr-substituted BFO samples having smaller nanoparticles in compared with BFO (see Table 1).

4 Summary

We have summarized the key points from our work on the Ce/Zr co-substituted BFO as follows: (1) The XRD and Raman spectroscopy studies confirmed that the samples are single phase even for the highest doping of 6% of Ce and Zr accompanied by a rhombohedral-tetragonal phase structural transition. (2) The lattice distortion observed in Ce/Zr co-substituted BFO accompanied by the anomalous enhancement of the A1–2 mode induces a magnetic anisotropy in $BiFeO_3$. (3) Increasing the Ce/Zr co-substitution decreases the values of crystalline size due to the increase of the compressive stress induced into the $BiFeO_3$ lattice, while it increases the particle size. (4) The bandgap energy significantly increases with the increasing of Ce/Zr co-substitution suggesting that the materials are suitable as UV and blue-green-driven photocatalysts, or optoelectronic devices. (5) The weak ferromagnetic behavior observed in Ce/Zr co-substituted samples is related to the following reasons: the destruction of a cycloidal antiferromagnetic structure of BFO due to the rhombohedral-tetragonal structural transition, and the exchange interaction between the 4f- and 3d magnetic orbitals of Ce^{3+} and Fe^{3+} ions.

References

1. J. Wang, H. Zheng, V. Nagarajan, B. Liu, S.B. Ogale, D. Viehland, V. Venugopalan, D.G. Schlom, M. Wutting, R. Ramesh, J.B. Neaton, U.V. Waghmare, N.A. Hill, K.M. Rabe, Epitaxial $BiFeO_3$ multiferroic thin film heterostructures. Science **299**, 1719–1722 (2003)
2. D. Lebeugle, D. Colson, A. Forget, M. Viret, Very large spontaneous electric polarization in $BiFeO_3$ single crystals at room temperature and its evolution under cycling fields. Appl. Phys. Lett. **91**(2), 022907 (2007)
3. W. Wei et al., The magnetoelectric coupling in rhombohedral–tetragonal phases coexisted $Bi_{0.84}Ba_{0.20}FeO_3$. Phys. B Condens. Matter **407**(12), 2243–2246 (2012)

4. B. Ruette et al., Magnetic-field-induced phase transition in $BiFeO_3$ observed by high-field electron spin resonance: cycloidal to homogeneous spin order. Phys. Rev. B **69**(6), 064114 (2004)
5. A. Mukherjee, S. Basu, L.A.W. Green, N.T.K. Thanh, M. Pal, Enhanced multiferroic properties of Y and Mn codoped multiferroic $BiFeO_3$ nanoparticles. J. Mater. Sci. **50**, 1891–1900 (2015)
6. R. Irandoust, A. Gholizadeh, A comparative study of the effect of the non-magnetic and magnetic trivalent rare-earth ion substitutions on bismuth ferrite properties: Correlation between the crystal structure and physical properties. Solid State Sci. **101**, 106142 (2020)
7. L. Esmaili, A. Gholizadeh, The effect of Nd and Zr co-substitution on structural, magnetic and photocatalytic properties of $Bi_{1-x}Nd_xFe_{1-x}Zr_xO_3$ nanoparticles. Mater. Sci. Semiconduct. Process. **118**, 105179 (2020)
8. M. Li, S. Yang, R. Shi, L. Li, R. Zhu, X. Li, Y. Cheng, X. Ma, J. Zhang, K. Liu, P. Yu, P. Gao, Engineering of multiferroic $BiFeO_3$ grain boundaries with head-to-head polarization configurations. Sci. Bull. (2020). https://doi.org/10.1016/j.scib.2020.12.032
9. F. Noori, A. Gholizadeh, Structural, optical, magnetic properties and visible light photocatalytic activity of $BiFeO_3$/-graphene oxide nanocomposites. Mater. Res. Express **6**, 1250 (2019). https://doi.org/10.1088/2053-1591/ab6807
10. X. Jiang, J. Sun, X. Chai, Y. Chen, W. Zhang, J. Jiang, A. Jiang, Large domain-wall current in $BiFeO_3$ epitaxial thin films. Ceram. Int. **47**, 10130–10136 (2021). https://doi.org/10.1016/j.ceramint.2020.12.161
11. P. Suresh, B.K. Hazra, B.R. Kumar, T. Chakraborty, P.D. Babud, S. Srinath, Lattice effects on the multiferroic characteristics of (La, Ho) co-substituted $BiFeO_3$. J. Alloys Compd. **863**, 158719 (2021)
12. M. Sahni, S. Mukhopadhyay, R.M. Mehra, S. Chauhan, P.C. Sati, M. Kumar, M. Singh, N. Kumar, Effect of Yb/Co co-dopants on surface chemical bonding states of BiFeO3 nanoparticles with promising photocatalytic performance in dye degradation. J. Phys. Chem. Solids **152**, 109926 (2021)
13. N.P. Samantray, R.N.P. Choudhary, Studies of structural, dielectric and impedance spectroscopy of Ca/Zr modified $BiFeO_3$ ceramics. Mater. Chem. Phys. **260**, 124115 (2021)
14. M. Akhtar, S. Saba, S. Arif, G.M. Mustafa, A. Khalid, G. Ali, S. Atiq, Efficient magnetoelectric dispersion in Ni and Co co-doped $BiFeO_3$ multiferroics. Physica B **602**, 412572 (2021)
15. R. Ahmed, R.J. Si, S. Rehman, Y. Yu, Q.J. Li, C. Wang, High dielectric constant and low temperature ferroelectric-phase-transition in Ca, Pb co-doped $BiFeO_3$. Results Phys. **20**, 103623 (2021)
16. Y. Li, L. Liu, D. Wang, H. Zhang, H. Zhang, X. He, Q. Li, The local structure and exchange bias effect of (Ho, Co)-codoped $BiFeO_3$ investigated by XAFS spectroscopy. Physica B **604**, 412709 (2021)
17. C. Tian, Q. Yao, Z. Tong, G. Rao, J. Deng, Z. Wang, J. Wang, H. Zhou, J. Zhao, The influence of Nd substitution on microstructural, magnetic, and microwave absorption properties of $BiFeO_3$ nanopowders. J. Alloys Compd **859**, 157757 (2021)
18. D.V. Karpinsky, A. Pakalniškis, G. Niaura, D.V. Zhaludkevich, A.L. Zhaludkevich, S.I. Latushka, M. Silibin, M. Serdechnova, V.M. Garamus, A. Lukowiak, W. Stręk, M. Kaya, R. Skaudžius, A. Kareiva, Evolution of the crystal structure and magnetic properties of Sm-doped $BiFeO_3$ ceramics across the phase boundary region. Ceram. Int. **47**, 5399–5406 (2021)
19. A.S. Naeimi, E. Dehghan, D. Sanavi Khoshnoud, A. Gholizadeh, Enhancment of ferromagnetism in Ba and Er co-doped $BiFeO_3$ nanoparticles. J. Magn. Magn. Mater. **393**, 502–507 (2015)
20. M. Arora, S. Chauhan, P.C. Sati, M. Kuma, Effect of non-magnetic ions substitution on structural, magnetic and optical properties of $BiFeO_3$ nanoparticles. J. Supercond. Nov. Magn. **27**, 1867–1871 (2014)
21. Z. Quan, Hu. Hao, Xu. Sheng, W. Liu, G. Fang, M. Li, X. Zhao, Surface chemical bonding states and ferroelectricity of Ce-doped $BiFeO_3$ thin films prepared by sol–gel process. J. Sol-Gel Sci. Technol. **48**, 261–266 (2008)
22. X. Zhang, M. Gao, Gu. Yueliang, H. Bao, X. Li, X. Zhou, W. Wen, The structure−property investigation of $Bi_{1-x}Ce_xFeO_3$ (x = 0, 0.05)−Li battery. In situ XRD and XANES studies. J. Phys. Chem. C **116**, 20230–20238 (2012)
23. J. Liu, M. Li, Z. Hu, L. Pei, J. Wang, X. Liu, X. Zhao, Effects of ion-doping at different sites on multiferroic properties of $BiFeO_3$ thin films. Appl. Phys. A **102**, 713–717 (2011)
24. Z. Quan, W. Liu, Hu. Hao, Xu. Sheng, B. Sebo, G. Fang, M. Li, X. Zhao, Microstructure, electrical and magnetic properties of Ce-doped $BiFeO_3$ thin films. J. Appl. Phys. **104**, 084106 (2008). https://doi.org/10.1063/1.3000478
25. M. Arora, M. Kumar, Structural, magnetic and optical properties of Ce substituted $BiFeO_3$ nanoparticles. Ceram. Int. **41**(4), 5705–5712 (2015)
26. E.M.M. Ibrahim, G. Farghal, M.M. Khalaf, H.M. Abd El-Lateef, Magnetic and DC electric properties of sol–gel-synthesized Ce-doped $BiFeO_3$ nanoflake. Appl. Phys. A **123**, 533 (2017)
27. P.C. Sati, M. Kumar, M. Arora, M. Tomar, V. Gupta, Effect of Zr substitution on structural, magnetic, and optical properties of $Bi_{0.9}Dy_{0.1}Fe_{1-x}Zr_xO_3$ multiferroic ceramics prepared by

rapid liquid phase sintering method. Ceram. Int. **43**, 4904–4909 (2017)
28. M. Kumar, M. Arora, S. Chauhan, S. Joshi, Raman spectroscopy probed spin-two phonon coupling and improved magnetic and optical properties in Dy and Zr substituted $BiFeO_3$ nanoparticles. J. Alloys Compd. **692**, 236–242 (2017)
29. J. Rodríguez-Carvajal, Recent developments of the program FULLPROF, in commission on powder diffraction (IUCr). Newsletter **26**, 12–19 (2001)
30. A. Gholizadeh, N. Tajabor, Influence of N_2- and Ar-ambient annealing on the physical properties of SnO_2:Co transparent conducting films. Mater. Sci. Semicond. Process. **13**, 162–166 (2010)
31. L. Venkidu, M.V.G. Babu, P.E. Rubavathi, B. Bagyalakshmi, B. Sundarakannan, Structure, microstructure, magnetic and magnetodielectric investigations on $BaTi_{(1-x-y)}Fe_xNb_yO_3$ ceramics. Ceram. Int. **44**, 8161–8165 (2018)
32. Y. Wang, C.-W. Nan, Site modification in BiFeO3 thin films studied by Raman spectroscopy and piezoelectric force microscopy. J. Appl. Phys. **103**, 114104 (2008)
33. J. Li, X.Y. Guan, Structural and optical properties of Ce doped $BiFeO_3$ nanoparticles via sol–gel method. Micro Nano Lett. **14**(13), 1307–1311 (2019)
34. J. Sharma, D. Basandrai, A.K. Srivastava, Ce Co-doped $BiFeO_3$ multiferroic for optoelectronic and photovoltaic applications. Chin. Phys. B **26**(11), 116201 (2017)
35. J.-P. Zhou, R.-J. Xiao, Y.-X. Zhang, Z. Shi, G.-Q. Zhu, Novel behaviors of single-crystalline $BiFeO_3$ nanorods hydrothermally synthesized under magnetic field. J. Mater. Chem. C **3**, 6924 (2015)
36. Y.Q. Jia, Crystal radii and effective ionic radii of the rare earth ions. J. Solid State Chem. **95**, 184–187 (1991)
37. R.D. Shannon, Revised effective ionic radii and systematic studies of interatomic distances in halides and chalcogenides. Acta Cryst. A **32**, 751–767 (1976)
38. A. Gholizadeh, A comparative study of physical properties in Fe_3O_4 nanoparticles prepared by coprecipitation and citrate methods. J. Am. Ceram. Soc. **100**(8), 3577–3588 (2017)
39. R. Naik, J.J. Nazarko, C.S. Flattery, U.D. Venkateswaran, V.M. Naik, M.S. Mohammed, G.W. Auner, J.V. Mantese, N.W. Schubring, A.L. Micheli, A.B. Catalan, Temperature dependence of the Raman spectra of polycrystalline $Ba_{1-x}Si_xTiO_3$. Phys. Rev. B **61**, 11367 (2000)
40. S. Chauhan, M. Kumar, P. Pal, Substitution driven structural and magnetic properties and evidence of spin phonon coupling in Sr-doped $BiFeO_3$ nanoparticles. RSC Adv. **6**, 68028–68040 (2016)
41. S. Chaturvedi, R. Bag, V. Sathe, S. Kulkarni, S. Singh, Holmium induced enhanced functionality at room temperature and structural phase transition at high temperature in bismuth ferrite nanoparticles. J. Mater. Chem. C **4**, 780–792 (2016)
42. M.M. Shirolkar, J. Li, X. Dong, M. Li, H. Wang, Controlling the ferroelectric and resistive switching properties of a $BiFeO_3$ thin film prepared using sub-5 nm dimension nanoparticles. Phys. Chem. Chem. Phys. **19**, 26085 (2017)
43. M.K. Singh, S. Ryu, H.M. Jang, Polarized Raman scattering of multiferroic $BiFeO_3$ thin films with pseudo-tetragonal symmetry. Phys. Rev. B **72**, 132101 (2005)
44. A. Gholizadeh, The effects of A/B-site substitution on structural, redox and catalytic properties of lanthanum ferrite nanoparticles. J. Mater. Res. Technol. **8**(1), 457–466 (2019)
45. A. Gholizadeh, A. Malekzadeh, M. Ghiasi, Structural and magnetic features of $La_{0.7}Sr_{0.3}Mn_{1-x}Co_xO_3$ nano-catalysts for ethane combustion and CO oxidation. Ceram. Int. **42**(5), 5707–5717 (2016)
46. A. Gholizadeh, H. Yousefi, A. Malekzadeh, F. Pourarian, Calcium and strontium substituted lanthanum manganite–cobaltite $[La_{1-x}(Ca, Sr)_xMn_{0.5}Co_{0.5}O_3]$ nano-catalysts for low temperature CO oxidation. Ceram. Int. **42**(10), 12055–12063 (2016)
47. W. Zhou, H. Deng, H. Cao, J. He, J. Liu, P. Yang, J. Chu, Effects of Sm and Mn co-doping on structural, optical and magnetic properties of $BiFeO_3$ films prepared by a sol–gel technique. Mater. Lett. **144**, 93–96 (2015)
48. D. Kuang, P. Tang, X. Wu, S. Yang, X. Ding, Y. Zhang, Structural, optical and magnetic studies of (Y, Co) co-substituted $BiFeO_3$ thin films. J. Alloy. Compd. **671**, 192–199 (2016)
49. A. Gholizadeh, A comparative study of the physical properties of Cu–Zn ferrites annealed under different atmospheres and temperatures: Magnetic enhancement of $Cu_{0.5}Zn_{0.5}Fe_2O_4$ nanoparticles by a reducing atmosphere. J. Magn. Magn. Mater. **452**, 389–397 (2018)
50. A. Gholizadeh, E. Jafari, Effects of sintering atmosphere and temperature on structural and magnetic properties of Ni–Cu–Zn ferrite nano-particles: magnetic enhancement by a reducing atmosphere. J. Magn. Magn. Mater. **422**, 328–336 (2017)
51. H. Khedri, A. Gholizadeh, Experimental comparison of structural, magnetic and elastic properties of $M_{0.3}Cu_{0.2}Zn_{0.5}Fe_2O_4$ (M = Cu, Mn, Fe Co, Ni, Mg) nanoparticles. Appl. Phys. A **125**, 709 (2019)
52. D. Wang et al., Sol–gel synthesis of Nd-doped $BiFeO_3$ multiferroic and its characterization. Ceram. Int. **41**, 8768–8772 (2015)
53. S. Godara, N. Sinha, B. Kumar, Study the influence of Nd and Co/Cr co-substitutions on structural, electrical and magnetic properties of $BiFeO_3$ nanoparticles. Ceram. Int. **42**(1), 1782–1790 (2016)

54. T. Wang, T. Xu, S. Gao, S.-H. Song, Effect of Nd and Nb co-doping on the structural, magnetic and optical properties of multiferroic $BiFeO_3$ nanoparticles prepared by sol-gel method. Ceram. Int. **43**, 4489–4495 (2017)

Terms and Conditions

Springer Nature journal content, brought to you courtesy of Springer Nature Customer Service Center GmbH (“Springer Nature”).
Springer Nature supports a reasonable amount of sharing of research papers by authors, subscribers and authorised users (“Users”), for small-scale personal, non-commercial use provided that all copyright, trade and service marks and other proprietary notices are maintained. By accessing, sharing, receiving or otherwise using the Springer Nature journal content you agree to these terms of use (“Terms”). For these purposes, Springer Nature considers academic use (by researchers and students) to be non-commercial.
These Terms are supplementary and will apply in addition to any applicable website terms and conditions, a relevant site licence or a personal subscription. These Terms will prevail over any conflict or ambiguity with regards to the relevant terms, a site licence or a personal subscription (to the extent of the conflict or ambiguity only). For Creative Commons-licensed articles, the terms of the Creative Commons license used will apply.
We collect and use personal data to provide access to the Springer Nature journal content. We may also use these personal data internally within ResearchGate and Springer Nature and as agreed share it, in an anonymised way, for purposes of tracking, analysis and reporting. We will not otherwise disclose your personal data outside the ResearchGate or the Springer Nature group of companies unless we have your permission as detailed in the Privacy Policy.
While Users may use the Springer Nature journal content for small scale, personal non-commercial use, it is important to note that Users may not:

1. use such content for the purpose of providing other users with access on a regular or large scale basis or as a means to circumvent access control;
2. use such content where to do so would be considered a criminal or statutory offence in any jurisdiction, or gives rise to civil liability, or is otherwise unlawful;
3. falsely or misleadingly imply or suggest endorsement, approval , sponsorship, or association unless explicitly agreed to by Springer Nature in writing;
4. use bots or other automated methods to access the content or redirect messages
5. override any security feature or exclusionary protocol; or
6. share the content in order to create substitute for Springer Nature products or services or a systematic database of Springer Nature journal content.

In line with the restriction against commercial use, Springer Nature does not permit the creation of a product or service that creates revenue, royalties, rent or income from our content or its inclusion as part of a paid for service or for other commercial gain. Springer Nature journal content cannot be used for inter-library loans and librarians may not upload Springer Nature journal content on a large scale into their, or any other, institutional repository.
These terms of use are reviewed regularly and may be amended at any time. Springer Nature is not obligated to publish any information or content on this website and may remove it or features or functionality at our sole discretion, at any time with or without notice. Springer Nature may revoke this licence to you at any time and remove access to any copies of the Springer Nature journal content which have been saved.
To the fullest extent permitted by law, Springer Nature makes no warranties, representations or guarantees to Users, either express or implied with respect to the Springer nature journal content and all parties disclaim and waive any implied warranties or warranties imposed by law, including merchantability or fitness for any particular purpose.
Please note that these rights do not automatically extend to content, data or other material published by Springer Nature that may be licensed from third parties.
If you would like to use or distribute our Springer Nature journal content to a wider audience or on a regular basis or in any other manner not expressly permitted by these Terms, please contact Springer Nature at

onlineservice@springernature.com